

## Insertion device for EUV-lithography at fourth-generation SR facility

© A.V. Murzina,<sup>1,2</sup> Ya.V. Rakshun,<sup>1,3</sup> Yu.V. Khomyakov,<sup>1</sup> V.A. Chernov<sup>1</sup>

<sup>1</sup> Budker Institute of Nuclear Physics, Siberian Branch, Russian Academy of Sciences, 630090 Novosibirsk, Russia

<sup>2</sup> Novosibirsk State University, 630090 Novosibirsk, Russia

<sup>3</sup> Siberian State University of Telecommunications and Information Science, 630102 Novosibirsk, Russia  
e-mail: a.murzina@g.nsu.ru

Received April 23, 2024

Revised April 23, 2024

Accepted April 23, 2024

This paper is dedicated to the optimization of the fourth-generation storage ring insertion devices for EUV lithography. Optimal period lengths have been determined, and the APPLE-II and Delta insertion devices have been compared in circular and linear polarization modes according to spectral, power characteristics, source size, and angular divergence. The average power values of the working harmonic have been obtained: about 6 W for circular polarization and about 2.6 W — for linear polarization. The coherent properties of the generated synchrotron radiation have been evaluated: the coherent fractions have been calculated, and transverse coherence functions have been obtained.

**Keywords:** Extreme ultra-violet lithography (EUVL), synchrotron radiation (SR), insertion device (ID), elliptical polarized undulator (EPU), partially coherent radiation.

DOI: 10.61011/TP.2024.08.58999.129-24

### Introduction

The miniaturization of microelectronics components enables the production compact low-power devices. One of the most promising areas for microelectronics is extreme ultraviolet lithography, which allows the creation of high-precision and high-density components. An important condition for the implementation of EUV-technology is the properties of the radiation source. There are various sources, including gas discharge, laser-plasma, liquid-jet-plasma sources, etc. The development of synchrotron radiation (SR) sources, namely the emergence of the 4th generation facilities with ultra-low-emittance storage rings, has resulted in them once again being able to successfully compete with conventional sources.

High photon flux density, the ability to produce spectrally narrow lines, and low angular divergence of radiation constitute a number of the advantages of 4th generation SR sources. In addition, the 4th-generation SR facility SKIF being under construction in Russia will have an emittance of  $\sim 75 \text{ pm} \cdot \text{rad}$  [2], which makes it extremely promising for EUV lithography applications. On the one hand, the properties of the source enhance the capabilities of high-precision X-ray optics with a large numerical aperture ( $\text{NA} \sim 0.3$ ) [3]. It is quite possible to achieve nanometer spatial resolution using such optics. On the other hand, the reduction of the size of the source allows increasing the power density in focus and thereby reducing the exposure time. Furthermore, the coherent flux of the fourth-generation SR source is comparable to the total photon flux

of the third-generation SR source, which leads to improved spatial resolution.

First of all, to design a synchrotron radiation (SR) facility appropriate for EUV lithography tasks, it is essential to select a light-generating insertion device, optimize its parameters, and obtain the final radiation characteristics. APPLE-II and Delta type undulators were considered in this paper in the modes of linear and circular light polarization, their parameters were optimized, and their spectral and power characteristics and angular divergence of radiation were compared. An equally important part of this work is the assessment of the coherent properties of the SR, which opens up the possibility for the subsequent design of the X-ray optical path of the experimental (and technological) station.

### 1. Requirements for insertion device

The fourth generation SR sources have high radiation brilliance, which, in particular, causes high thermal loads on the optics. At the same time, the quality of optics is crucial for achieving high spatial resolution parameters in EUV lithography. A solution that allows for a spatial separation of radiation by harmonics is the generation of radiation with circular polarization. In this case, the fundamental harmonic of the undulator spreads along its axis, and all other harmonics spread in a cone around this axis, which fundamentally reduces the thermal load on the optics. On the other hand, in some cases it would be useful to receive linearly polarized radiation beams on the axis, which leads

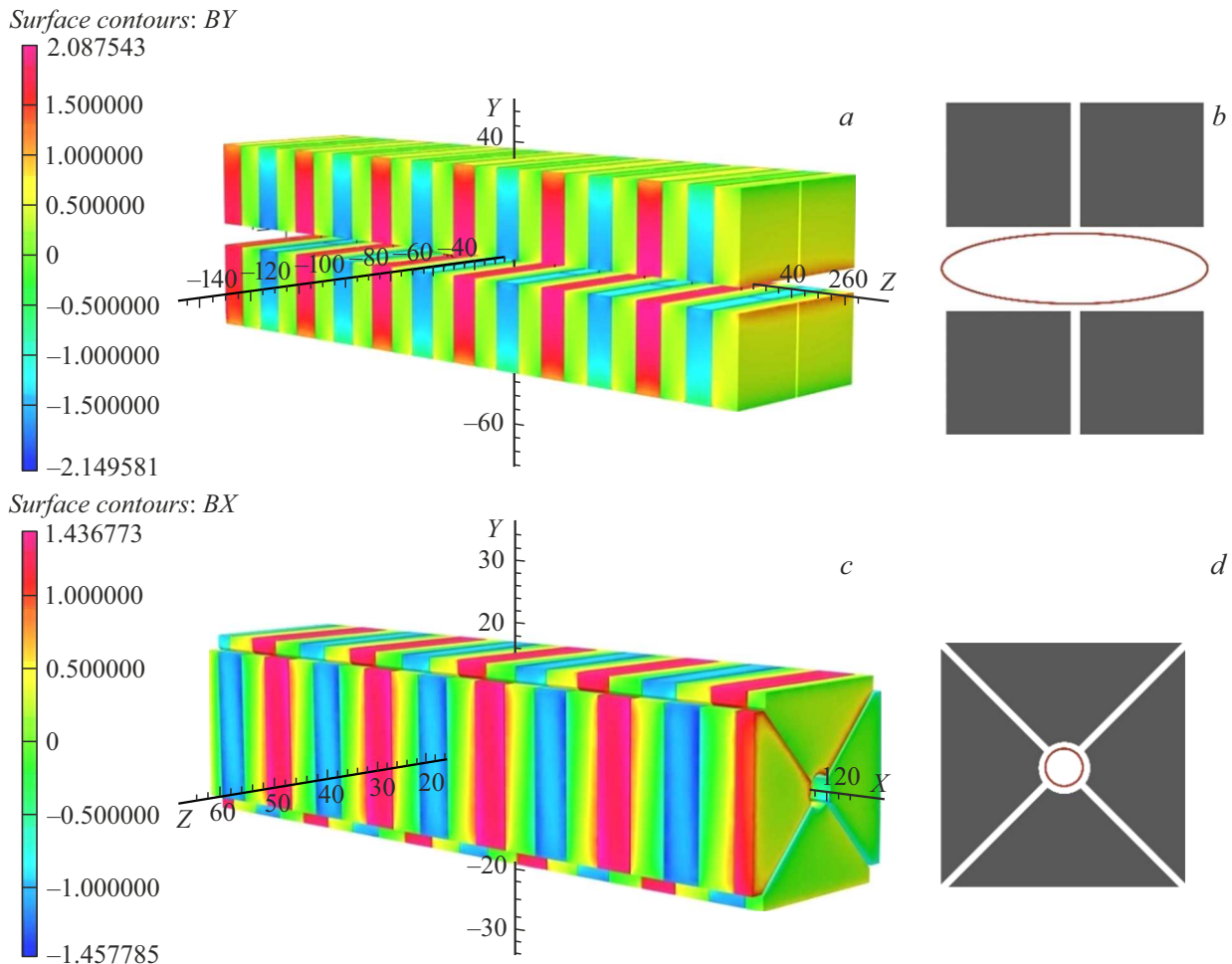


**Figure 1.** Permanent magnet undulators: *a* — magnetic structure of the APPLE-II type undulator; *b* — view of the end of the APPLE-II type undulator, where the vacuum chamber is marked in red; *c* — magnetic structure of the Delta type undulator; *d* — view of the end of the Delta type undulator, where the vacuum chamber is marked in red.

to the need to change the type of polarization of the generated radiation. The most technologically advanced and widely utilized type of insertion device for polarization switching is the APPLE-II undulator, which has proven itself at the 4th generation MAX-IV facility. A Delta-type undulator is another option worth considering [5]. It should be noted that it is also desirable that the spectral width of the undulator harmonic corresponds to the spectral bandwidth of the focusing mirrors used.

## 2. Optimization of insertion devices

In general, APPLE-type insertion devices consist of four magnetic arrays that can be longitudinally shifted relative to each other, thereby controlling the polarization of the emitted radiation. Each array contains repeating periods with four different magnet orientations. Various models of APPLE-type undulators differ in the shape of magnetic arrays and their mutual arrangement, as well as the direction of magnetization in periodic blocks. All these factors, in

turn, affect a number of design parameters, for example, the device and shape of the vacuum chamber, which can be both inside and outside the insertion device.

The APPLE-II type undulator (Fig. 1, *a*) consists of four parallel magnet arrays arranged in pairs above and below the vacuum chamber. Thus, the vacuum chamber is always located inside the insertion device and takes an elongated (traditional) shape in cross section (Fig. 1, *b*).

The magnetic structure of the Delta type undulator (Fig. 1, *c*) can be considered as a combination of two identical planar undulators rotated by  $90^\circ$  relative to each other around the beam axis. On the other hand, it can also be considered as a kind of APPLE-III type structure. The specific shape of the magnet arrays makes it possible to reduce the magnitude of the vertical gap and, accordingly, increase the amplitude of the magnetic field. The vacuum chamber inside the Delta type insertion device has a circular cross section (Fig. 1, *d*), however, since both the magnitude of the magnetic field and the polarization change due to the longitudinal shift of the magnetic arrays[6], it is also possible to place an insertion device inside the vacuum chamber.

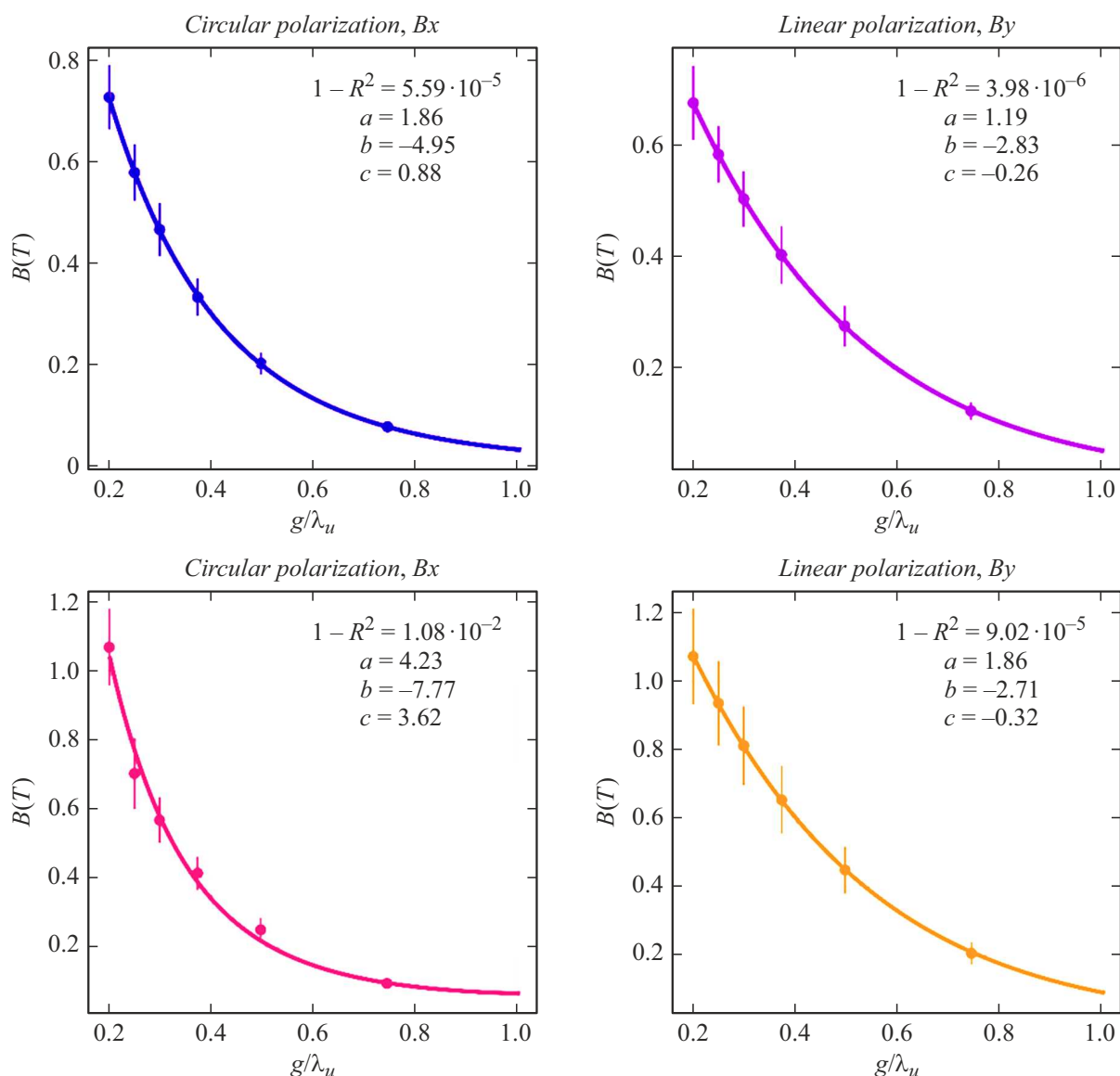


**Figure 2.** The dependence of the peak magnetic field on the ratio of the vertical gap to the period for an APPLE-II type undulator in the case of circular and linear polarization. The points on the graph correspond to the results of numerical simulation. The quality of the approximation is characterized by the criterion  $R^2$ , the value of  $1-R^2$  is given for ease of interpretation.

40SH NdFeB with residual magnetization  $B_r = 1.26$  T was selected as the material of undulator magnets as one of the most technologically advanced, affordable materials with resistance to degradation under ionizing radiation conditions [7].

In order to optimize these devices for the tasks of EUV lithography, it is necessary to formulate requirements for the wavelength of fundamental undulator harmonic, considering the possibilities of optics and at the same time targeting for the maximum photon flux at operational energy. An instance of high numerical aperture optics for EUV lithography is the Schwarzschild lens, which is based on normal incidence multilayer mirrors. The most important advantage of such mirrors is the ability to capture the entire useful harmonic of radiation from an undulator

with  $dE/E$  of the order of 1%. One of the ways to achieve high spatial resolution in EUV is to reduce the wavelength of the radiation. At the same time, however, it should be noted that beamline optics are required to effectively reflect this radiation, since several mirrors are always used in optical systems for EUV lithography. At the moment, the technology of sputtering of multilayer coatings allows producing X-ray mirrors of normal incidence over a wavelength range up to 3 nm [8]. Nonetheless, a more conservative variant with an 11 nm wavelength (112.7 eV) is taken as the main one in this work, and the insertion devices' parameters are optimized for it.

For this purpose, a magnetostatic calculation was performed, which allows moving from the magnetic structure and design features of undulators to a set of parameters

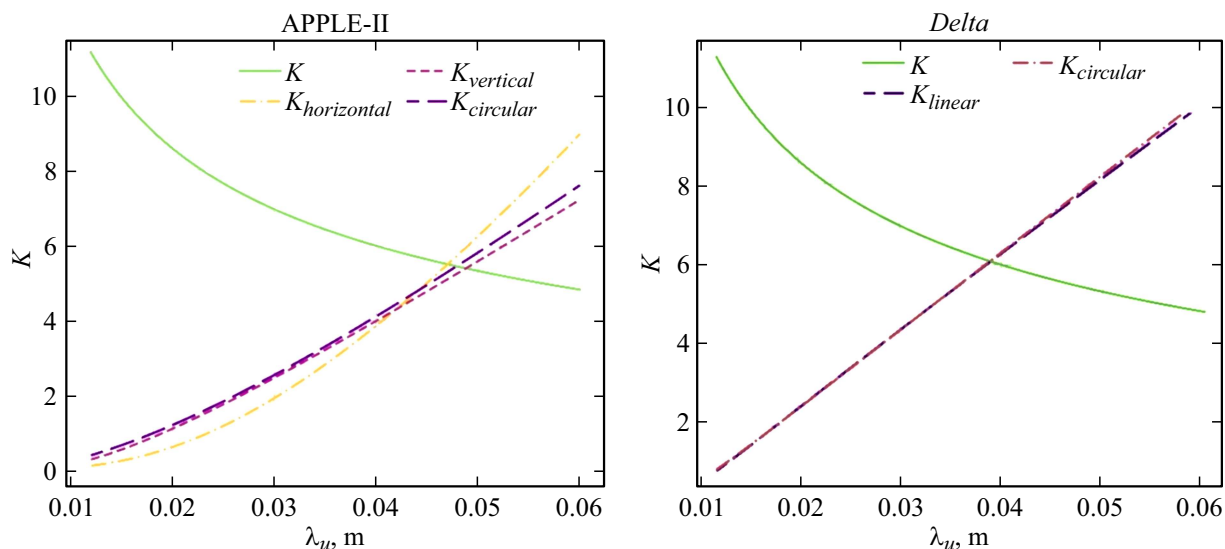


**Figure 3.** Optimization of the period length of APPLE-II type undulators (left) and Delta (right) at a fixed wavelength of the fundamental harmonic 11 nm. Solid line shows the dependence corresponding to equation (3); dashed and dotted lines represent the dependencies corresponding to equation (2) in the circular and in linear, specifically, horizontal and vertical radiation polarization modes.

**Table 1.** Characteristics of the APPLE-II insertion device used for magnetostatic calculation

Width of magnetic blocks, mm	Height of magnetic blocks, mm	Horizontal gap between a pair of magnetic arrays, mm
30	30	0.1

related to radiation generation. The parameters used in the simulation are given in Table 1. The magnetic field was computed for an APPLE-II type undulator using the finite element method in the OPERA 3D [9] program.

The magnitude of the peak magnetic field in APPLE undulators is related to the relative distance between the lower and upper pairs of magnetic arrays (with vertical gap) and is determined by the relation [10]:

$$B = a \exp[b(g/\lambda_u) + c(g/\lambda_u)^2], \quad (1)$$

where  $B$  — peak magnetic field on the undulator axis,  $g$  — vertical gap value,  $\lambda_u$  — undulator period length,  $a, b, c$  — numerical coefficients.

It is necessary to approximate the results of numerical simulation of the peak magnetic field from the parameter  $g/\lambda_u$  to determine the unknown dependence coefficients. To accomplish this, the peak magnetic field with a fixed period along the axis of the insertion device was calculated at various vertical gap values by averaging modulo the local extremes of each field component.

The dependence of the peak field on the period of the undulator with calculated coefficients  $a, b, c$  is shown in Fig. 2. As depicted in the figure, a high field value on the undulator axis is achieved by increasing the period of

the magnetic structure at a fixed gap. However, an increase of the period of the magnetic field results in a decrease of the number of poles, since the length of the undulator is limited by the length of the storage ring's straight sections. The reduction of the number of poles ultimately decreases the generated photon flux.

Thus, it is necessary to strive to minimize the vertical gap while taking into account the design features of the undulator, and to optimize the magnetic period with a fixed gap. There is a design limitation associated with the presence of a vacuum chamber inside the device for APPLE-II type undulators. A minimum gap value of 8 mm was selected for SKIF after a number of discussions and consultations in the Budker Institute of Nuclear Physics of the Siberian Branch of the Russian Academy of Science.

When optimizing the parameters of the insertion device, it is convenient to consider the deflection parameter defined by the equation

$$K = e\lambda_u B(\lambda_u)/(2\pi m_e c), \quad (2)$$

where  $e$  — electron charge,  $m_e$  — electron mass,  $c$  — speed of light,  $B(\lambda_u)$  — peak magnetic field associated with the undulator period by the relation (1).

On the other hand, the constructive interference condition links the parameter  $K$  with the undulator period.

$$m\lambda_m = \lambda_u/(2\gamma^2)(1 + K^2/2), \quad (3)$$

where  $\lambda_m$  — the wavelength of radiation at the  $m$ th harmonic of radiation, and  $\gamma$  — the Lorentz factor.

A graphical representation of these two types of relation is shown in Fig. 3. The intersection of the curves uniquely determines the optimal value of the period length, which was 50 mm for an undulator of the APPLE-II type.

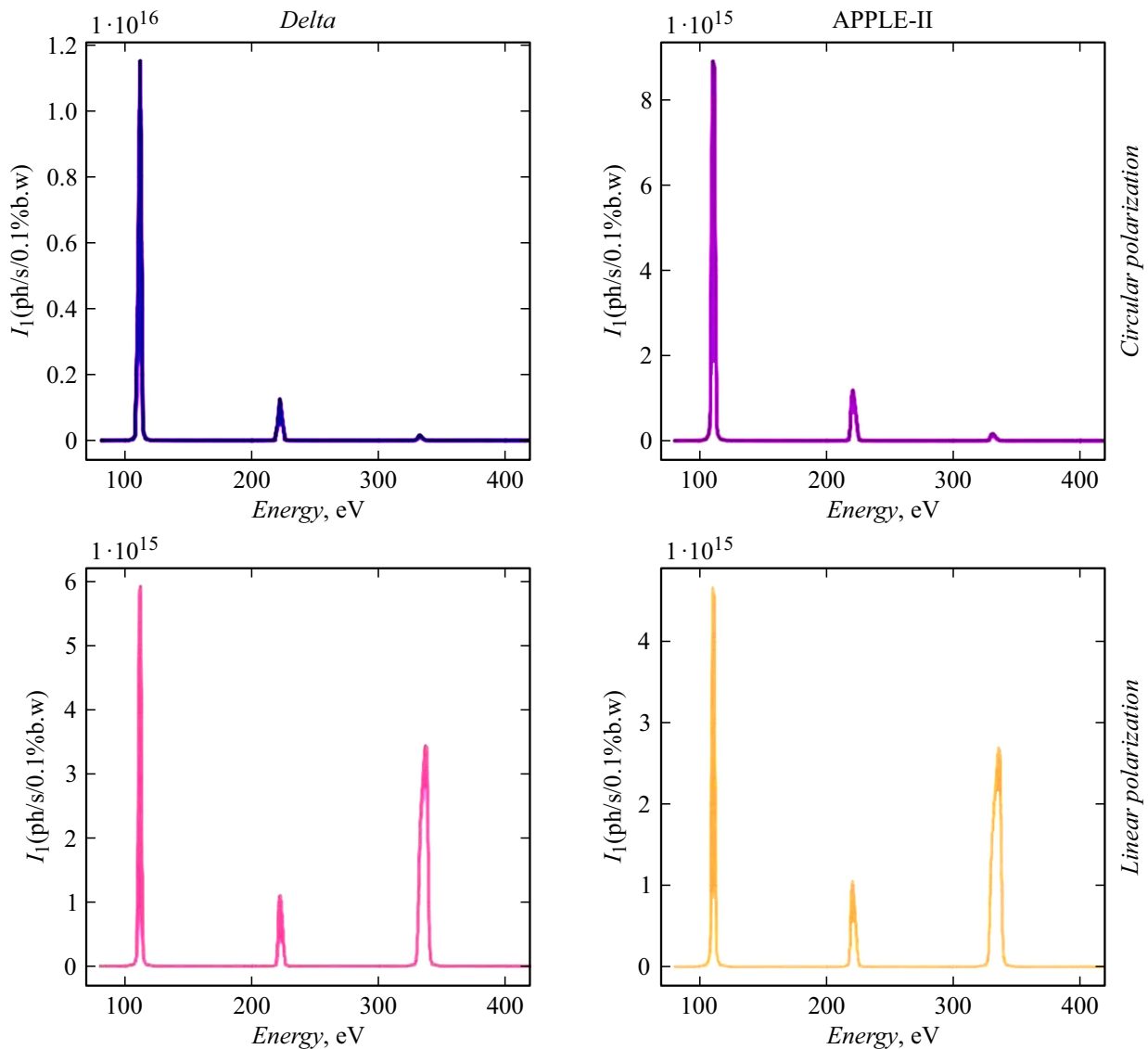


**Figure 4.** Spectra on the axis of APPLE-II and Delta type undulators in circular and linear polarization modes with fundamental harmonic energy 112.7 eV.

The coefficients of the ratio (1) for the Delta undulator with N40SH magnet material were calculated in the original article [5], devoted to the description of the insertion device design. The optimal period length for the Delta type undulator was 40 mm after optimization performed in a similar way. At the same time, the option of intra-vacuum placement of magnetic poles was considered, in which the minimum gap value is 5 mm.

### 3. Characteristics of the generated radiation

The spectral characteristics of the radiation generated by the optimized devices were calculated using the code SPECTRA [11]. The value calculated in the previous section was chosen as the undulator period, the length

of the magnetic structure was assumed to be 5 m which is the maximum possible length for the undulator in the straight section of the storage of SKIF facility (the length of the rectilinear straight section is 6 m). The storage ring parameters are listed in Table 2.

The calculated spectral densities of the photon flux on the axis at a fixed energy of the fundamental harmonic  $E_1 = 112.7$  eV and envelopes of the angular spectral density of the photon flux for undulators of the APPLE-II and Delta types are shown in Fig. 4 and 5. It should be noted that the fundamental harmonic of radiation propagates along the axis of the undulator in both linear and circular polarization modes, whereas all other harmonics in the circular polarization mode have their maxima off-axis, and the intensity of their radiation on the axis is significantly lower (Fig. 4). At the same time, the first harmonic has

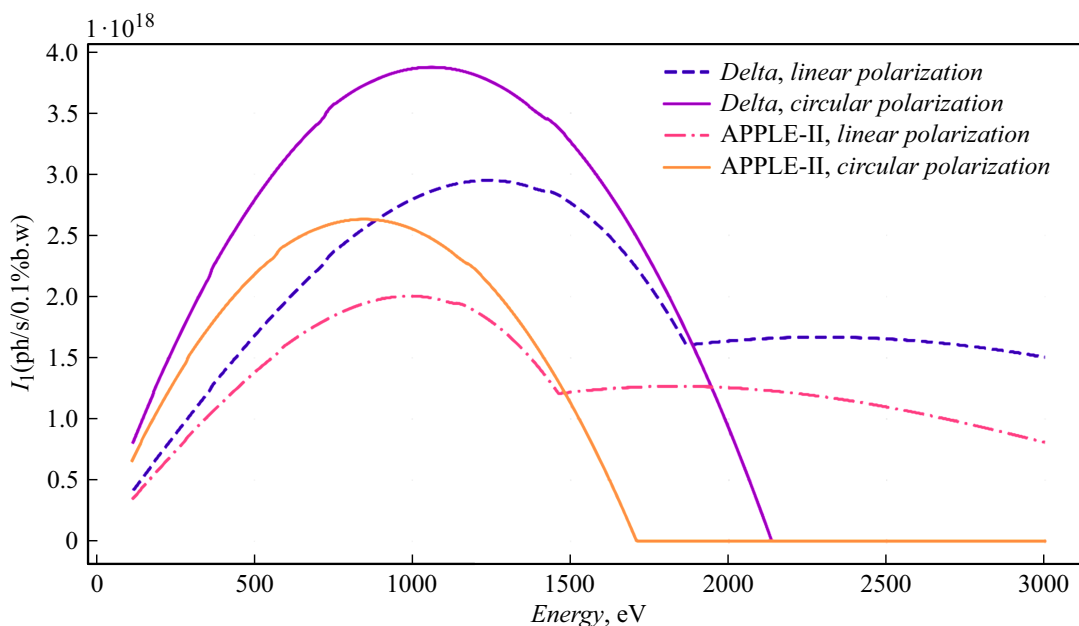


**Figure 5.** Envelopes of the angular spectral density of the photon flux of APPLE-II and Delta type undulators in circular and linear polarization modes.

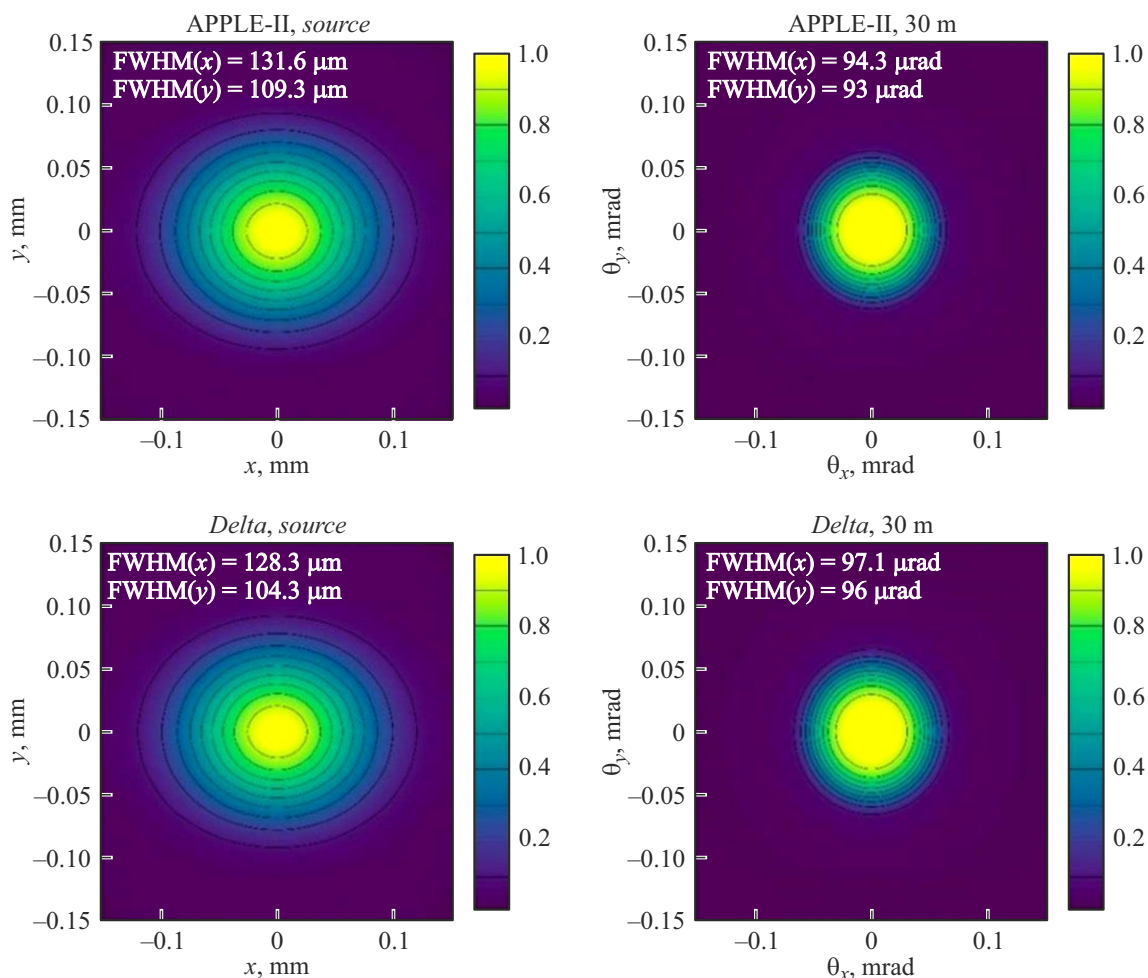


**Figure 6.** Source sizes and angular divergences at a distance of 30m from the source in an incoherent approximation for APPLE-II and Delta undulators.

**Table 2.** Parameters of the storage ring of SKIF facility [12] used in radiation modeling

Energy of electrons, GeV	Beam current, mA	Circumference, m	Natural emittance, pm-rad	Horizontal beta function in the center straight section, m	Vertical beta function in the center straight section, m
3	400	476	75	15.6	2.37

the highest spectral angular density of the photon flux, and the photon flux density in the circular polarization mode is twice as high as in the linear polarization mode.

The angular spectral density of the photon flux of the Delta type undulator is higher than that of the APPLE-II type undulator (Fig. 5) in the entire range of the first harmonic energy tuning due to the smaller vertical gap. However, it can be seen that undulators of both types are quite suitable for generating radiation in a wide range of soft X-rays (from 100 to 1500–2000 eV) and can be used to solve other problems.

When calculating in detail the radiation characteristics of insertion devices such as APPLE-II and Delta, it should be taken into account that it is already possible for third-generation sources to reach the diffraction limit in the vertical direction, and ignoring the wave properties of radiation can result in errors [13]. Moreover, wave properties should be taken into account when considering radiation from forth-generation SR sources.

Even so, as a zero approximation, it is possible to simulate radiation without reckoning for coherent properties in order to obtain estimated characteristics. This approach is based on the model implemented in the SPECTRA software. The final emittance and energy spread of the radiation is taken into account in this approach by convolution of the Gaussian distribution of electrons in the beam with the distribution of the radiation intensity of one electron, neglecting the interference of electron fields [11].

The ability to estimate the coherent fraction is also implemented in SPECTRA. The horizontal and vertical „coherent fractions“ for optimized insertion device are presented in Table 3.

Figure 6 shows the characteristic sizes and angular divergences of the radiation beam at a distance of 30 m from the source in an incoherent approximation for APPLE-II and Delta type undulators calculated using SPECTRA. In the presented and subsequent calculations, a circular aperture with a diameter of  $6\sigma$  corresponding to the first harmonic of radiation ( $\pm 3\sigma$  relative to the center of the beam, with the full width at half maximum  $\text{FWHM} = \sqrt{8 \ln 2} \sigma \approx 2.355\sigma$ ) was used. For ease of comparison, maxima of the intensity distribution are set to 1, and the FWHM value for each of the distribution projections is indicated.

High coherent fraction (Table. 3) allows for the use of a fully coherent approximation, in which radiation is emitted by a single electron with zero emittance. Figure 7 shows the

**Table 3.** The coherent fractions of optimized insertion devices

Insertion device	Horizontal coherent fraction	Vertical coherent fraction
APPLE-II	0.58	0.92
Delta	0.56	0.89

radiation beam sizes and angular divergences at a distance of 30 m from the source in the one-electron approximation, calculated also using SPECTRA.

It is necessary to take into account the partial coherence of the radiation for a more accurate calculation. A number of methods are used for modeling partially coherent radiation. These approaches, are based, for example, on the decomposition of the transverse coherence function into fully coherent Gauss–Schell modes (decomposition by Hermite polynomials) [14]. However, in the case when the coherent fraction is high, this consideration has serious drawbacks due to the functions describing the behavior of undulator radiation at the source and in the far region are not Gaussian in nature. Far-field electric radiation field strength at a resonant frequency  $\omega$  of the fundamental harmonic can be expressed as follows [13]:

$$\begin{aligned} \bar{E}_{\perp}(z_0, \boldsymbol{\eta}_k, \mathbf{l}_k, \boldsymbol{\theta}) = & -\omega e A_{JJ} L K / (\gamma 2c^2 z_0) \exp[i\omega z_0 |\boldsymbol{\theta}| \\ & - (|\mathbf{l}_k / z_0|^2 / (2c))] \text{sinc}[\omega L |\boldsymbol{\theta}| - (|\mathbf{l}_k / z_0| - \boldsymbol{\eta}_k)^2 / (4c)], \quad (4) \end{aligned}$$

where  $\boldsymbol{\eta}_k$  and  $\mathbf{l}_k$  — deflection angle and coordinate of the  $k$ th electron,  $\boldsymbol{\theta} = \mathbf{r} / z_0$ ,  $z_0$  — the point at which the radiation is recorded,  $L$  — the length of the undulator,  $A_{JJ} = J_0(\xi) - J_1(\xi)$  and  $\xi = K^2 / (4 + 2K^2)$  — the longitudinal coordinate.

The alternative method used in this work is as follows: first, it generates the electron distribution within a single electron bunch (in realization); next, it combines fields of the form (4) from each electron in this realization; and at last, the sum averages over all realizations. This approach was implemented using OCELOT [15] code. To obtain information about the distribution of radiation intensity in the source, the virtual source method is used, propagating radiation from the far field region to the center of the undulator. Then the expression for the imaginary source

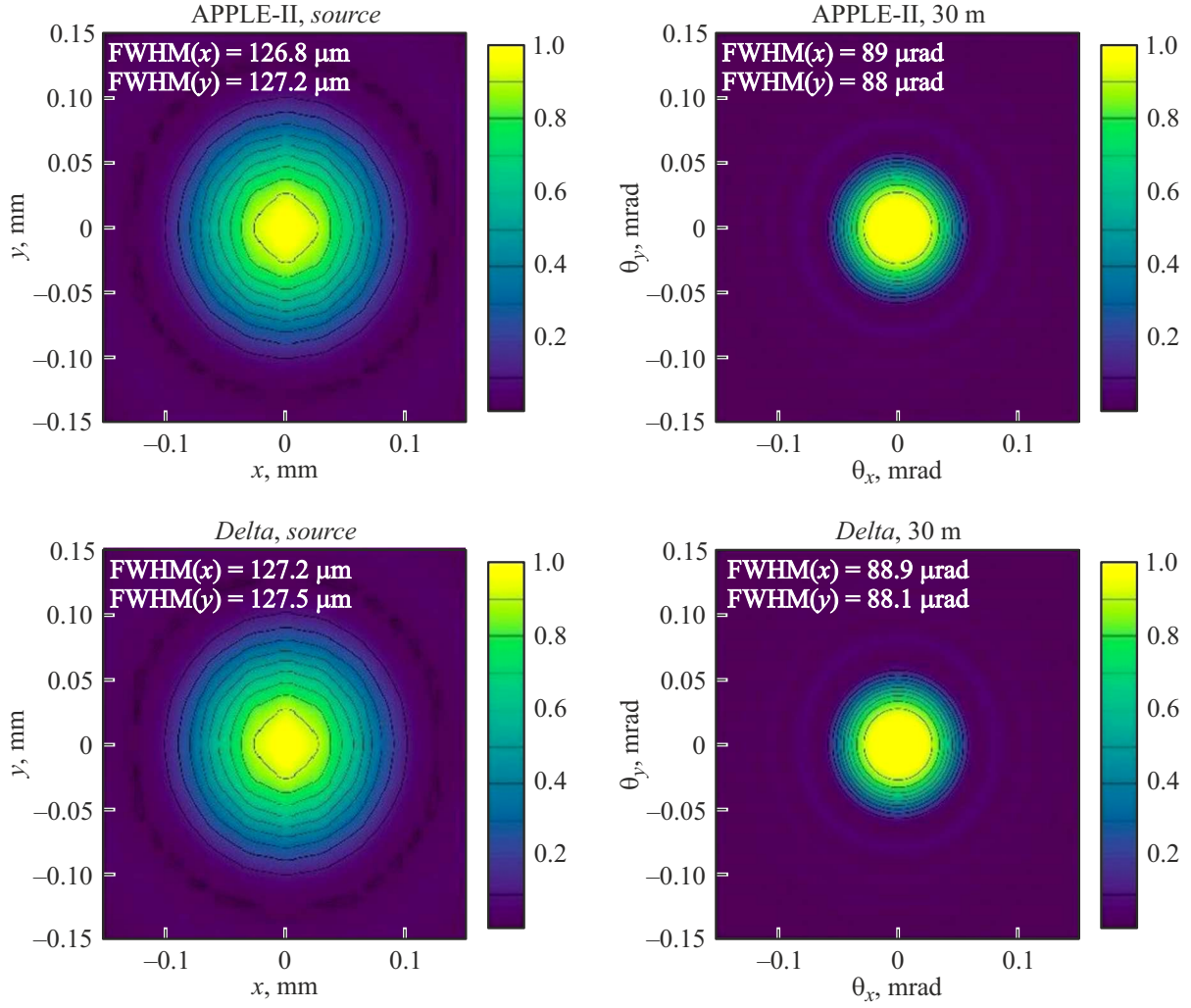


**Figure 7.** Source sizes and angular divergences at a distance of 30 m from the source in the approximation of single electron radiation for APPLE-II and Delta undulators in linear and circular polarization mode.

has the following form

$$\begin{aligned} \bar{E}_{\perp}(0, \boldsymbol{\eta}_k, \mathbf{l}_k, \boldsymbol{\theta}) &= i\omega eA_{JJ}K/(2\gamma c^2) \exp\left[i\frac{\omega}{c}\boldsymbol{\eta}_k(\mathbf{r}_{\perp} - \mathbf{l}_k)\right] \\ &\times [\pi - 2\text{Si}(i\omega|\mathbf{r}_{\perp} - \mathbf{l}_k|^2/(Lc))]. \end{aligned} \quad (5)$$

Ultimately, the complete information about the coherent properties of radiation is provided by the cross-spectral density or the transverse coherence function, which is actually a correlation function of the field:

$$\Gamma_{\perp}(\mathbf{r}_1, \mathbf{r}_2, \omega, z) = \langle E^*(\mathbf{r}_1, \omega, z)E(\mathbf{r}_2, \omega, z) \rangle. \quad (6)$$

In the expression (6)  $\langle \dots \rangle$  — averaging over an ensemble of realizations of spectral amplitudes of a monochromatic field  $\bar{E}(\mathbf{r}, \omega, z)$ .

It should be noted that in the general case of partially polarized and partially coherent radiation, a matrix consisting of cross-spectral functions of the electric field

components [16] should be introduced:

$$\hat{J}(\mathbf{r}_1, \mathbf{r}_2, z) = \begin{pmatrix} \Gamma_{xx}(\mathbf{r}_1, \mathbf{r}_2, z) & \Gamma_{xy}(\mathbf{r}_1, \mathbf{r}_2, z) \\ \Gamma_{yx}(\mathbf{r}_1, \mathbf{r}_2, z) & \Gamma_{yy}(\mathbf{r}_1, \mathbf{r}_2, z) \end{pmatrix}, \quad (7)$$

$$\Gamma_{\alpha\beta}(\mathbf{r}_1, \mathbf{r}_2, z) = \langle E_{\alpha}^*(\mathbf{r}_1, t, z)E_{\beta}(\mathbf{r}_2, t, z) \rangle.$$

In the case of linear polarization, there is one component of the field and only one nonzero component of the matrix (7). There are two perpendicular and uncorrelating components of the field propagated independently in the case of circular polarization. The case of circular polarization can be considered similarly to the case of linear polarization by representing them in the basis of left or right polarization  $\bar{E}_{RL} = \bar{E}_x \pm i\bar{E}_y$ .

Figure 8 shows the maximum normalized intensity distributions of partially coherent radiation of one field component, as well as the phase patterns at the source and in the far region for APPLE-II and Delta undulators. The figure also shows the FWHM values for all projections of intensity distributions.

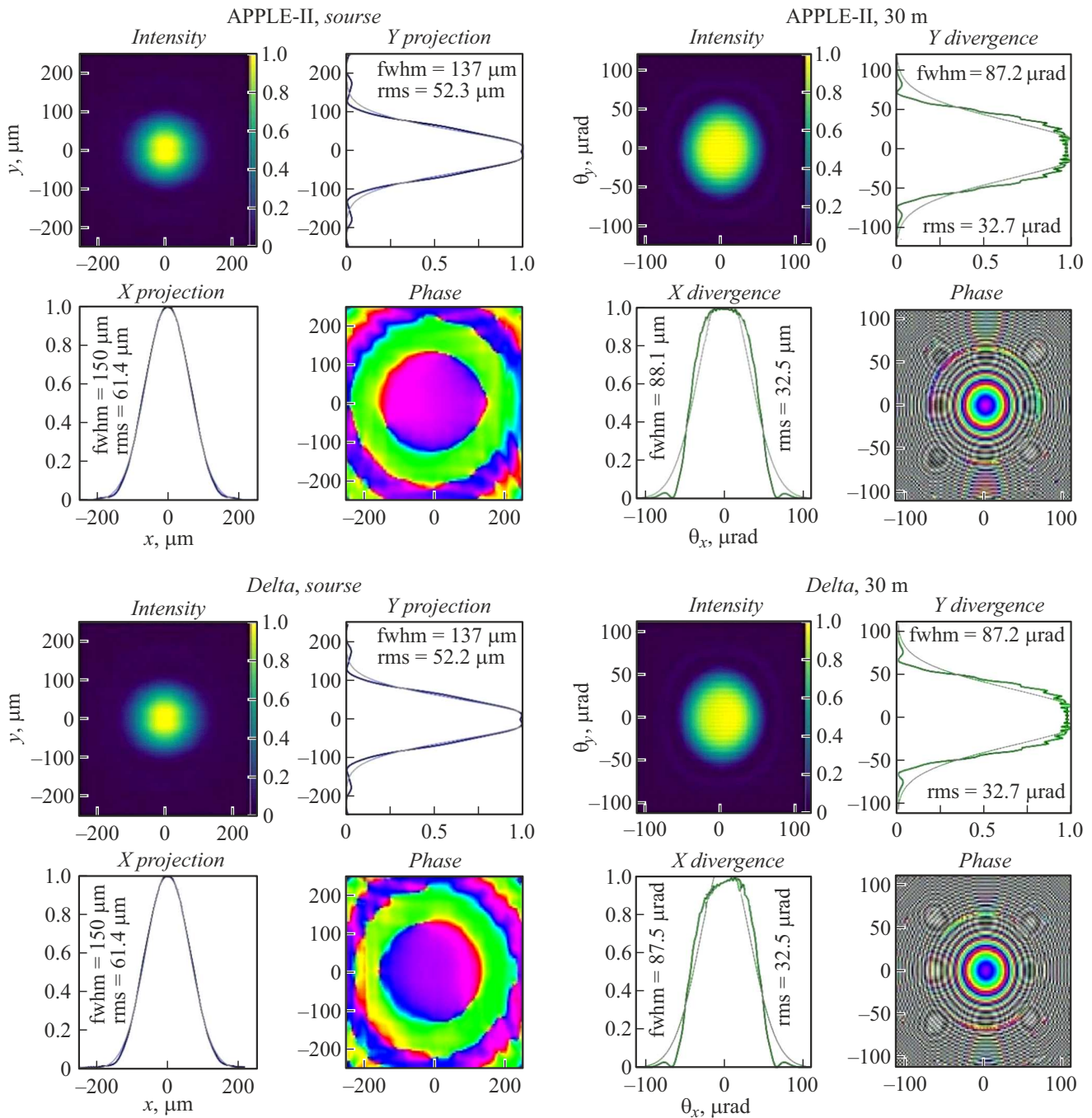


**Figure 8.** Normalized intensity distributions of a partially coherent beam for APPLE-II and Delta type undulators, their projections and phase patterns at a virtual source and in the far zone at a distance of 30 m.

Figure 9 shows the unit-normalized distributions (modulus squared) of the cross-spectral density (6) together with phase patterns for one component of the radiation field generated by APPLE-II and Delta type undulators at the source and in the far field region. These distributions fully characterize the coherent properties of the generated radiation.

The applicability of each method for determining the radiation parameters can be concluded with knowledge of the coherent fraction of photons and the FWHM

values for each distribution in the fully coherent and incoherent radiation approaches. Despite the fact that each of the methods showed an insignificant difference, it can be seen that in cases where the coherent fraction is high, the results of calculating the radiation of one electron closely resemble the calculated values for a partially coherent beam; conversely, when the coherent fraction is smaller, the results of incoherent calculation are closest to the values of FWHM in partially coherent radiation.

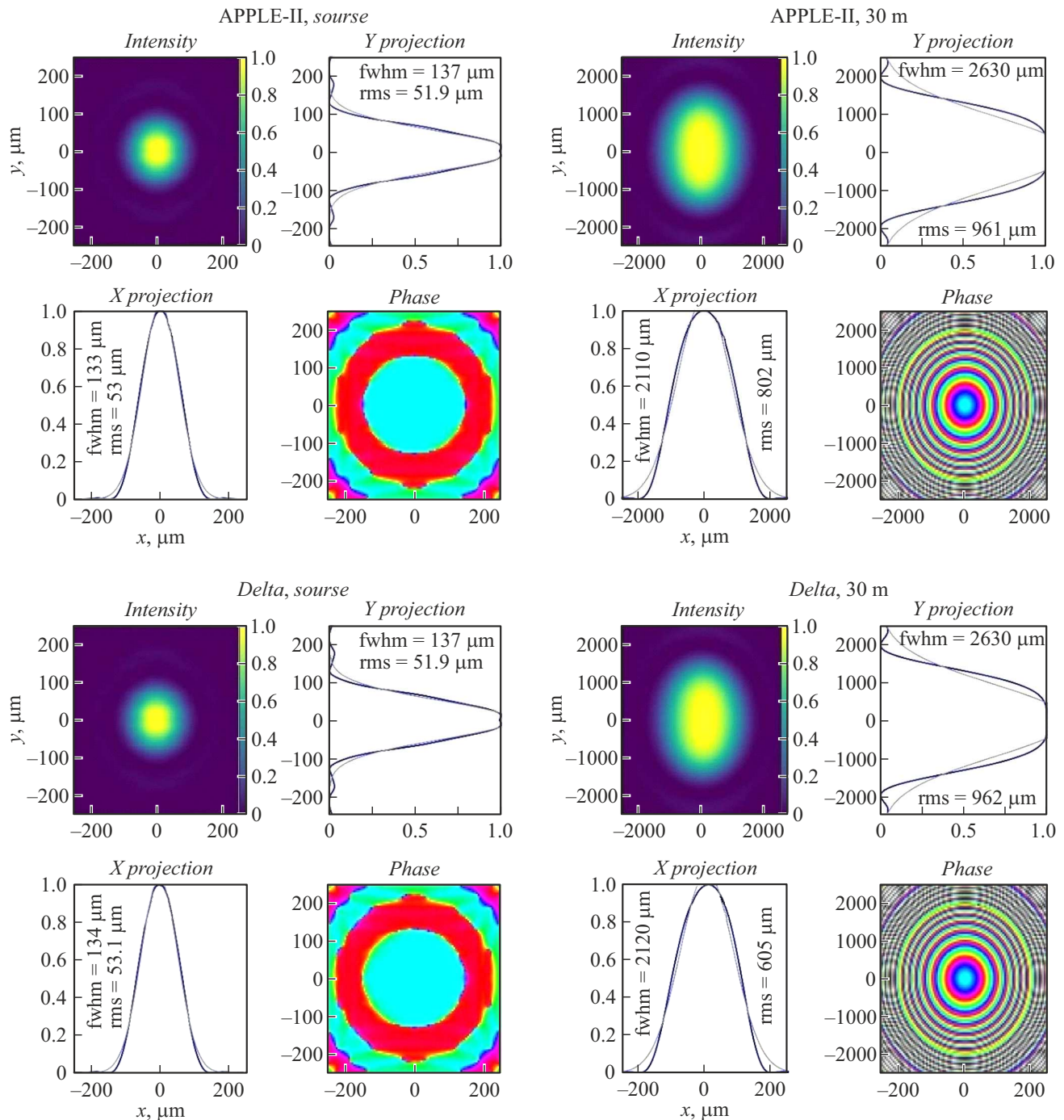


**Figure 9.** Distributions of the normalized transverse coherence function for APPLE-II and Delta type undulators at the virtual source and in the far field region.

Power density maps calculated using SPECTRA are shown in Fig. 10. The power passing through the aperture in the circular polarization mode for an APPLE-II type undulator is 5.72 W, and for a Delta type undulator — 6.12 W. In the linear polarization mode, the power passing through the aperture for an APPLE-II type undulator is 1.24 kW, for a Delta type undulator — 2.32 kW, while the transmitted power of the operational harmonic in each of the undulators is 2.53 and 2.58 W respectively.

The first optical element of the beamline receives high-power radiation in the linear polarization mode, which essentially results in difficulties in cooling and preserving an undistorted wavefront. In the circular polarization mode, the aperture transmits all the useful power of the first harmonic, filtering out the parasitic power of higher harmonics that are not used in experiments, which allows for further matching of the thermal and optical properties of the beamline optics for EUV lithography.

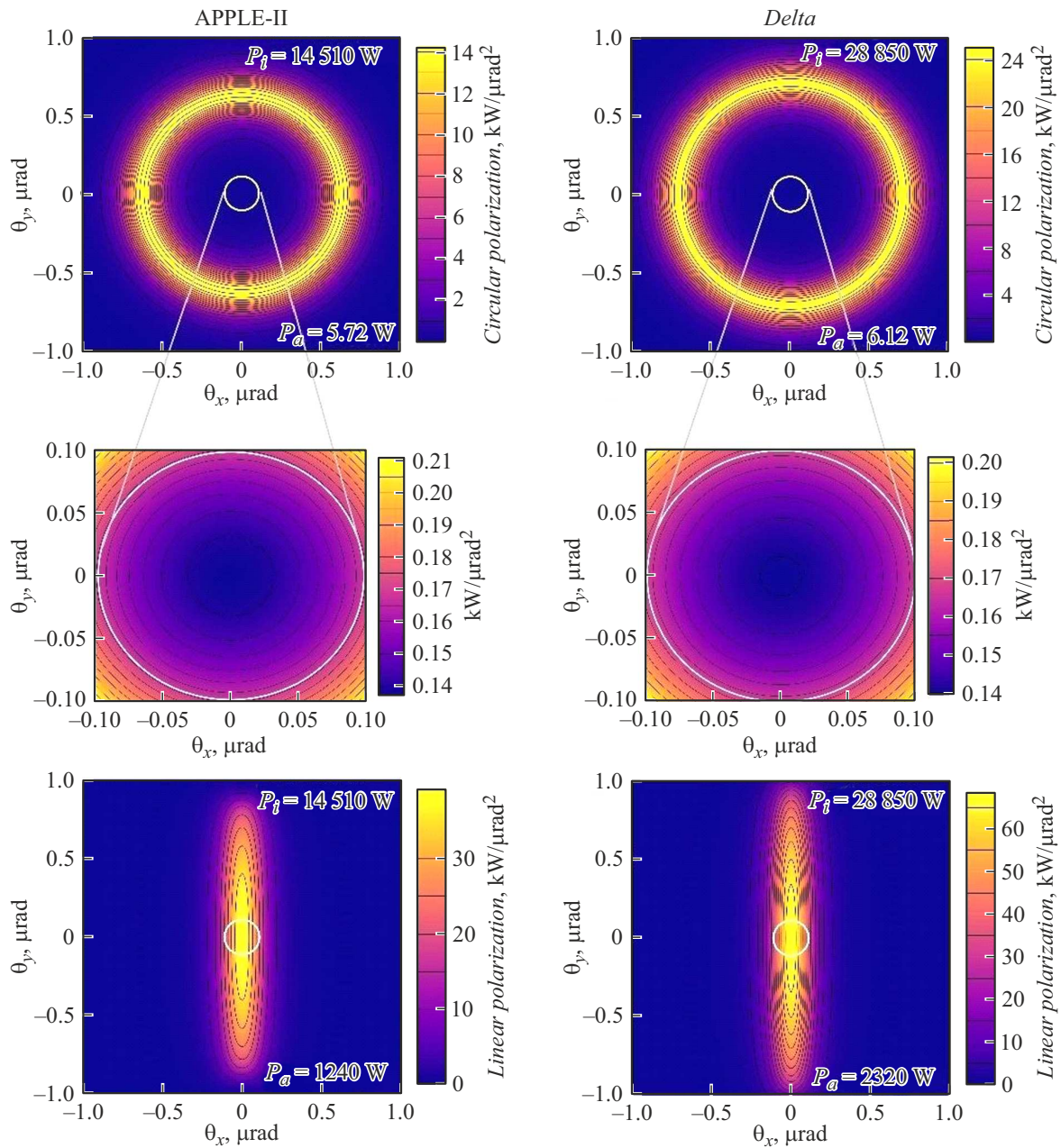


**Figure 10.** Power density maps for APPLE-II and Delta undulators in circular and linear polarization modes. The integral power  $P_i$  and the power  $P_a$  passed through the aperture  $6\sigma_{x,y}$  marked with a white border are indicated.

## Conclusion

The paper describes the requirements for an undulator that can be used for EUV lithography tasks at the 4th-generation SR facility using the example of a SKIF. Variants of usage of APPLE-II and Delta type undulators with permanent magnets are proposed. Based on the optimization of the magnetic period length, the spectral characteristics, as well as the parameters of the generated radiation in the far region and at the source, were determined using geometrical and wave optics approaches, which showed quite consistent results. In addition, power density maps

were obtained, the values of total and partial (apertured) power were determined. It was shown that the circular polarization mode is extremely promising for matching the thermophysical and X-ray optical parameters of optics.

## Acknowledgments

The authors would like to thank A.A. Starostenko, T.V. Rybitskaya, V.A. Pavlyuchenko for valuable advice on the application of methods for calculating magnetic systems, A.E. Trebushinin for his help in understanding algorithms for modeling partially coherent radiation, as well as E.B. Levichev and N.A. Mezentssev for a number of

important discussions regarding the design features of SKIF SR facility.

### Conflict of interest

The authors declare that they have no conflict of interest.

### References

- [1] B. Hansson. *Laser-Plasma Sources for Extreme-Ultraviolet Lithography* (Fysik, Stockholm, 2003)
- [2] E.B. Levichev, A.N. Zhuravlev, K.V. Zolotarev, Ya.V. Zubavichus, K.I. Schaefer. *Tekhnologicheskaya infrastruktura sibirskogo kol'tsevogo istichnika fotonov SKIF*, **1**, 8 (2022) (in Russian).
- [3] N.I. Chkhalo, N.N. Salashchenko. *J. Surf. Investig.*, **17**, 307 (2023). DOI: 10.1134/S1027451022060349
- [4] A. Thiel, M. Ebbeni, H. Tarawneh. *Veritas*, **48**, 6 (2018). DOI: 10.18429/JACoW-MEDSI2018-TUOPMA04
- [5] A.B. Temnykh. *Phys. Rev. ST Accel. Beams*, **11** (12), 120702 (2008). DOI: 10.1103/PhysRevSTAB.11.120702
- [6] R. Carr. *Nucl. Instr. Meth.*, **306** (1–2), 391 (1991). DOI: 10.1016/0168-9002(91)90346-R
- [7] A.B. Temnykh. *Nucl. Instr. Meth.*, **587** (1), 13 (2008). DOI: 10.1016/j.nima.2008.01.002
- [8] M.M. Barysheva, A.E. Pestov, N.N. Salashchenko, M.N. Toropov, N.I. Chkhalo. *Phys. Usp.*, **55** (7), 681 (2012). DOI: 10.3367/UFNc.0182.201207c.0727
- [9] OPERA. *Elektromagnitnaya i elektromekhanicheskaya simulyaciya*. URL: <https://www.3ds.com/ru/produkty-i-uslugi/simulia/produkty/opera/> (date of access: 02.03.2024)
- [10] T. Meinander. *CAS CERN Accelerator School: 5th General Accelerator Physics Course Proc.* (CERN, Geneva, 1994), v. 2, p. 983.
- [11] T. Tanaka, H. Kitamura. *J. Synchrotron Rad.*, **8** (6), 1221 (2001). DOI: 10.1107/S090904950101425X
- [12] A.V. Akimov, Yu.S. Aktershev, V.V. Anashin, A.V. Andiyarov, O.V. Anchugov, M.V. Arcentyeva, P.A. Bak, G.N. Baranov, A.M. Barnyakov, A.M. Batrakov, O.V. Belikov, L.L. Belova, E.A. Bekhtenev, V.I. Bukhtiyarov, A.V. Bogomyakov, V.M. Borin, D.B. Burenkov, D.S. Vinnik, V.N. Volkov, E.S. Vonda, K.M. Gorchakov, K.A. Grishina, D.S. Gurov, G.A. Gusev, B.A. Dovzhenko, E.N. Dementyev, A.I. Erokhin, A.A. Zharikov, K.V. Zhilyaev, A.A. Zhukov, A.N. Zhuravlev, K.V. Zolotarev, N.A. Zolotukhina, Ya.V. Zubavichus, S.E. Karnaev, G.V. Karpov, K.Yu. Karyukina, V.D. Kashkin, V.A. Kiselev, V.V. Kobets, E.S. Kotov, V.Ya. Korchagin, A.A. Krasnov, V.S. Krapivin, S.A. Krutikhin, V.S. Kuzminykh, G.N. Kulipanov, I.V. Kuptsov, G.Ya. Kurkin, A.E. Levichev, E.B. Levishev, D.V. Leshonok, (Dorokhova), P.V. Logachev, Yu.I. Maltseva, Ma Syao Chao, N.A. Mezentsev, O.I. Meshkov, N.V. Mityanina, I.A. Morozov, A.A. Morsin, S.A. Nikitin, D.A. Nikiforov, B.K. Ovchar, I.N. Okunev, A.V. Pavlenko, O.A. Pavlov, A.Yu. Pakhomov, V.M. Petrov, S.L. Pivovarov, P.A. Piminov, A.V. Polyansky, D.N. Pureskin, D.F. Reshetov, V.V. Repkov, E.A. Rotov, T.V. Rybitskaya, S.L. Samoilov, I.K. Sedlyarov, A.M. Semenov, D.V. Sen'kov, L.E. Serdakov, Sh.R. Signatulin, S.V. Sinyatkin, M.A. Skamarokha, A.A. Starostenko, A.G. Tribendis, A.V. Utkin, M.G. Fedotov, A.S. Tsyganov, A.D. Shiyankov, D.A. Shvedov, V.A. Shkaruba, K.S. Shtro, N.S. Shchegolkov. *Tekhnologicheskaya infrastruktura sibirskogo kol'tsevogo istichnika fotonov „SKIF“*, **2**, 98 (2022) (in Russian).
- [13] G. Geloni, E. Saldin, E. Schneidmiller, M. Yurkov. *Nucl. Instr. Meth.*, **588** (3), 463 (2008). DOI: 10.1016/j.nima.2008.01.089
- [14] T. Tanaka. *Opt. Lett.*, **42** (8), 1576 (2017). DOI: 10.1364/OL.42.001576
- [15] I. Agapov, G. Geloni, S. Tomin, I. Zagorodnov. *Nucl. Instr. Meth.*, **768**, 151 (2014). DOI: 10.1016/j.nima.2014.09.057
- [16] F. Gori, M. Santarsiero, S. Vicalvi, R. Borghi, G. Guattari. *Pure Appl. Opt.*, **7** (5), 941 (1998). DOI: 10.1088/0963-9659/7/5/004

Translated by A.Akhtyamov